Differential absorption saturation in laser cooled Yb:LiYF4

Long Cheng, Laura Andre, Gabriela Almeida, Luis H.C. Andrade, Sandro Lima, Junior Silva, Tomaz Catunda, Yannick Guyot, Stephen Rand

Optical Materials 128 (2022) 112404

Contents lists available at ScienceDirect

Optical Materials

journal homepage: www.elsevier.com/locate/optmat

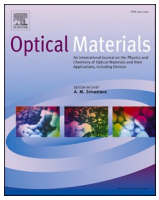

Differential absorption saturation in laser cooled Yb:$LiYF_4$

Long Cheng [a,*], Laura B. Andre [a], Gabriela L. Almeida [b], Luis H.C. Andrade [b], Sandro M. Lima [b], Junior R. Silva [b], Tomaz Catunda [c], Yannick Guyot [d], Stephen C. Rand [a]

[a] EECS Department, University of Michigan, Ann Arbor, MI, USA, 48105
[b] Programa em Recursos Naturais, Universidade Estadual de Mato Grosso do Sul, Dourados, Brazil
[c] Instituto de Física de São Carlos, Universidade de São Paulo, São Carlos, SP, Brazil
[d] Institut Lumiere Matiere, Universite Claude Bernard de Lyon 1, Lyon, France

ARTICLE INFO

Keywords:
Laser cooling
Yb:$YLiF_4$
Background absorption saturation
Radiation-balanced laser

ABSTRACT

The cooling efficiency for optical refrigeration by anti-Stokes Fluorescence was measured in a 10% Yb^{3+}:$LiYF_4$ crystal by Differential Luminescence Thermometry (DLT) and Thermal Lens Spectroscopy (TLS) over a range of pump intensities. Results showed that background and coolant ion absorption coefficients saturated at low intensities, and saturated differently as a function of wavelength. For wavelengths longer than 1000 nm, a higher pump intensity led to improved cooling efficiency through a differential saturation phenomenon. In this range, background absorption saturated more easily than the absorption of coolant ions so that parasitic heating was diminished, yielding higher cooling efficiency for higher pump intensities. This saturation phenomenon therefore offers the prospect of improved performance of electronic devices such as imaging arrays in space which could operate with reduced noise at low temperatures through laser cooling. The measured cooling efficiency was independent of pump intensity at a wavelength of 1000 nm where the saturation intensity of background absorption was found to be the same as that of Ytterbium in $LiYF_4$. A novel experimental method for determining the saturation intensities of impurity and coolant ions is described, and consequences for laser cooling and radiation-balanced laser operation of the observed saturation effects are discussed and analyzed.

1. Introduction

Laser cooling research based on anti-Stokes fluorescent (ASF) emission has witnessed steady growth and progress since the first experiment in 1995 [1]. Complementary methods of thermometry based on thermal cameras, differential luminescence and thermal lens spectroscopy have been introduced, and the search for better materials [2] for implementing optical refrigeration has led to important advances. Temperatures in the cryogenic range have been reached [3], the first all-optical cryocooler was demonstrated recently [4], and radiation-balanced lasers have moved from concept to reality [5–8]. Nevertheless, the purity of laser cooling materials [9] continues to be a key issue determining cooling efficiency in any given material. Unintentional impurities can absorb pump light or fluorescence, causing heating rather than cooling. To date, the theory of laser cooling has assumed that impurity absorption is a fixed property of a sample once it is grown. Consequently it has been thought that the only way to improve cooling efficiency was through sample purification. However this overlooks the possibility that background impurity absorption could be intensity dependent in a beneficial way. In this paper, we report the first observation of background absorption saturation in ASF cooling and demonstrate that this effect improves the cooling efficiency near room temperature at high pump intensities. Furthermore, an extension of existing theory of radiation-balanced lasers to include saturable parasitic heating is formulated which alters the predicted radiation-balance condition significantly.

Background impurity absorption is conventionally modeled as a constant versus wavelength and intensity, an assumption stemming from its presumed association with allowed transitions of certain dominant impurities. The main impurities of concern are unintended rare earth dopants and trace levels of transition metal ions. Strategies to improve laser cooling by curtailing the absorptive heatloads from these species have therefore focused on the obvious benefit of reducing impurity concentrations in laser cooling materials through strenuous purification efforts. Here an alternative way to decrease the parasitic heating caused by impurities in laser cooling experiments is examined,

* Corresponding author.
E-mail address: lonche@umich.edu (L. Cheng).

https://doi.org/10.1016/j.optmat.2022.112404
Received 24 February 2022; Received in revised form 23 March 2022; Accepted 23 April 2022
Available online 29 April 2022

one that reduces the background absorption relative to absorption by coolant ions through optical saturation. This approach relies on the wavelength dependence of saturation and exploits the difference in saturated absorption properties of various ions in the cooling medium.

Transition metals are thought to be important sources of background absorption in rare earth crystals, and Fe^{2+} and Fe^{3+} ions have been identified as the most prevalent impurity in Yb^{3+}:$LiYF_4$ [10]. Allowed infrared transitions of iron should generally have much higher saturation intensities [9] than the forbidden transitions of Yb^{3+} due to higher transition strength, even if they are detuned from resonance in the spectral region of our experiments. Consequently it has been deemed unlikely that the absorption of common impurities could saturate at a lower intensity than the coolant ion Yb^{3+}, as needed to improve cooling efficiency [11]. However, this overlooks the issue of impurity valence which greatly influences the optical properties of impurities. In particular, it overlooks the existence of stable valences of transition metal ions that have forbidden transitions in the optical range that could saturate as easily, or perhaps more easily, than Yb^{3+}. Trivalent iron provides an important example of a prevalent impurity with a low saturation intensity owing to such transitions. Moreover, because saturation intensity is in general wavelength-dependent, some interplay between coolant and impurity ion absorption at wavelengths might influence laser cooling at high intensities.

Saturation properties of Yb^{3+}:$LiYF_4$ were therefore investigated using thermal lens and differential luminescence spectroscopy to determine whether saturation effects of Yb^{3+} or background impurities, or both, can lead to improved laser cooling near room temperature. Experimentally, a novel technique for determining saturation intensities was uncovered and cooling efficiency was shown to improve at elevated pump intensity for wavelengths longer than 1000 nm. In this wavelength range, the increased saturation intensity of the Yb^{3+} coolant ions surpassed the saturation intensity of background impurities, which improved cooling efficiency and diminished parasitic heating with increasing pump intensity. Higher cooling efficiencies at long wavelengths were shown to be in agreement with theoretical estimates based on literature values of the saturation parameters of Fe^{3+} impurities but were at variance with the parameters for other valences of iron. This suggests that in Yb^{3+}:$LiYF_4$ the trivalent state of this dominant impurity can account for observed cooling behavior versus pump intensity. Finally, when two-species saturation takes place, a rate equation for impurity dynamics must be added to existing RBL theory [5–8]. Steady-state analysis of impurity saturation then predicts significant alterations in the radiation-balance condition for self-cooled lasers.

2. Theory

2.1. Saturation effects in laser cooling

The absorption of light by cooling ions and background impurities strongly affects the efficiency of laser cooling by the ASF method, but in opposite ways. At appropriate pump wavelengths, coolant ions with high radiative efficiency contribute to cooling by emitting at a wavelength shorter than that of the absorbed photons on average. Absorption by other impurities causes heating because their transitions are not part of the pump-driven cooling cycle but they typically undergo some non-radiative processes that generate heat. In this section the difference between coolant and background absorption (differential absorption) is analyzed as a function of intensity to reveal that the heatload can be reduced in materials where the background impurity absorption happens to saturate at a lower intensity than the cooling ions. Additional details on the impact of optical saturation on laser cooling efficiency are presented in the Appendices. The next section applies this concept to radiation-balanced lasers.

In early experiments the expression for cooling efficiency η_c was derived for a 2-level model [12] since experiments focused on Yb^{3+} ions which consist of ground and excited state manifolds $^2F_{7/2}$ and $^2F_{5/2}$ respectively. Possible intensity dependence of the background absorption was ignored since it was assumed to originate from allowed transitions of TM ions having very high saturation intensities. To include background saturation in the model, η_c can be derived in the customary way as the ratio of cooling power, P_c, to absorbed power, P_{abs} , only with intensity-dependent absorption coefficients.

$$\eta_c = \frac{P_c}{P_{abs}} = \eta_{ext}\frac{\lambda}{\lambda_f}\left[\frac{1}{1+\alpha_b(I)/\alpha_r(I)}\right] - 1 \tag{1}$$

The external quantum efficiency η_{ext} is the product of fluorescence escape efficiency η_e and the internal quantum efficiency η_{QE}. λ and I are the wavelength and intensity of the pump laser. In anisotropic media, the mean fluorescence wavelength λ_f must be determined from polarization-averaged emission spectra. The intensity dependence of the absorption coefficients ($\alpha_r(I)$ for the coolant ions and $\alpha_b(I)$ for background impurities) was assumed to have the form $\alpha(I) = \alpha(0)/(1 + I/I_{sat})$, where the saturation intensity I_{sat} was assigned the values $I_r(\lambda)$ or $I_b(\lambda)$ for coolant or background respectively [13].

In general, saturation intensity varies with wavelength. This is because it depends on detuning from resonance. Formally, this dependence can be expressed in terms of cross sections, which for coolant ions yields

$$I_r(\lambda) = \frac{hc}{\lambda\tau_f[\sigma_a(\lambda)+\sigma_e(\lambda)]} \tag{2}$$

where τ_f is the fluorescence lifetime. Here $\sigma_a(\lambda)$ is the effective absorption cross section which can easily be measured experimentally. The effective emission cross section $\sigma_e(\lambda)$ was calculated in a way that took into account the multiple Stark levels of Yb^{3+} and the Boltzman population distribution among them using the McCumber relation [14]. Fig. 1 displays both the effective cross sections for the 10% Yb^{3+}:$YLiF_4$ crystal studied in our experiments and the mean fluorescence wavelength of 997.6 nm. Together with an Yb^{3+} fluorescence lifetime of 2.2 ms [15], these quantities determine the theoretical saturation intensity of Yb^{3+} coolant ions in Eq. (2) which is plotted versus wavelength in Fig. 2. If we surmise for a moment that Fe^{3+} is the main background impurity species [10], with a broadband spectrum centered around 1 μm [16], the saturation intensity I_b would be only weakly wavelength-dependent

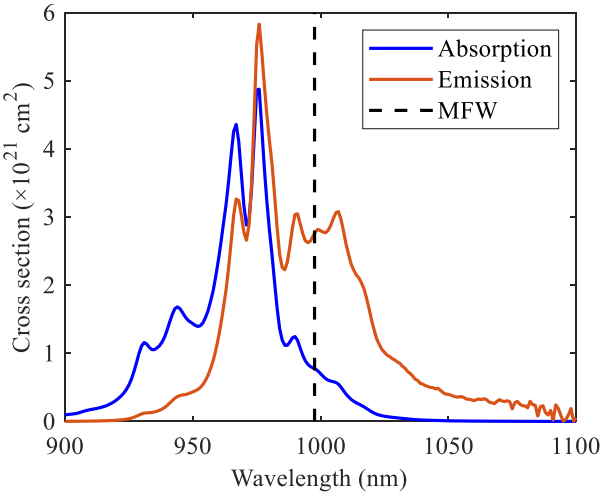

Fig. 1. Polarized absorption and emission cross sections of Yb:$LiYF_4$. Both spectra were recorded for E parallel to the 5.1 mm edge of the sample (see Supplemental Information for the precise orientation of crystal axes). The experimental absorption cross section (blue) was measured with a spectrophotometer. The effective emission cross section was calculated from McCumber theory [14]. As indicated by the dashed line, the polarization-averaged, mean fluorescence wavelength was 997.6 nm.

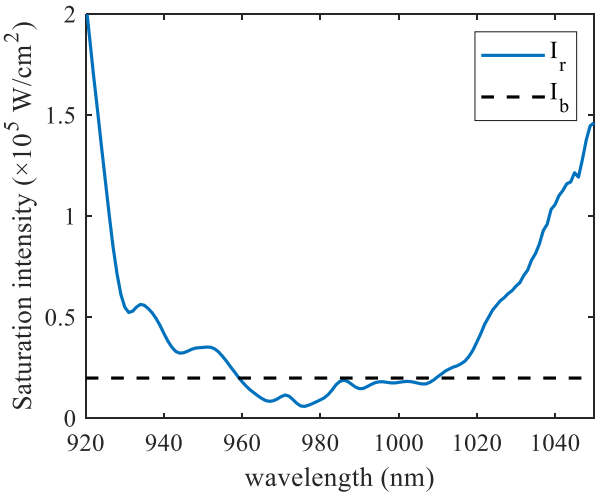

Fig. 2. Saturation intensities of Yb^{3+} and background absorption calculated from Eq. (2), illustrating different wavelength dependences. The solid curve (blue) is the saturation intensity I_r of Yb^{3+} while the dashed curve is I_b for background impurities exhibiting an intersection point at $\lambda_{cr} = 1010$ nm on the low energy side of the Yb^{3+} absorption band, where $I_b = I_r(\lambda_{cr}) = 3 \times 10^4\ W/cm^2$.

over the range of our experiments, unlike I_r which varies strongly with detuning. Under these circumstances, as outlined next, an experimental estimate of I_b can be determined that is illustrated as the dashed line in Fig. 2.

A plot of cooling efficiencies calculated from Eq. (1) using the two intensities $I = 3 \times 10^2\ W/cm^2$ and $I = 3 \times 10^4\ W/cm^2$ is shown in Fig. 3. At long wavelengths (>1 μm) the cooling efficiency is seen to increase at higher pump intensity. This unusual intensity dependence is readily explained by the background impurities being easier to saturate than coolant ions at large detunings from the Yb^{3+} absorption resonance displayed in Fig. 1. In this range, saturation of background absorption

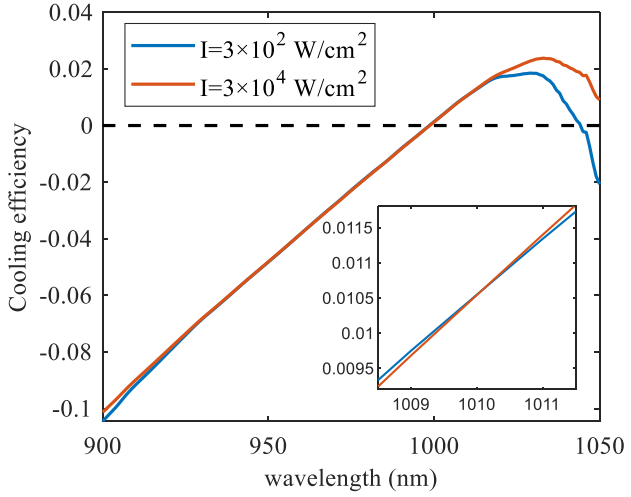

Fig. 3. Cooling efficiency from Eq. (1) versus wavelength at pump intensities differing by two orders of magnitude. Cooling efficiency curves predicted at high and low intensity (red and blue respectively) on the low energy side of 1010 nm where intersection occurs. A background saturation intensity of $3 \times 10^4\ W/cm^2$ was estimated from the wavelength $\lambda_{cr} = 1010$ nm of the crossing point (see inset) using Eq. (2). Note that in the cooling range the high intensity cooling efficiency exceeds the low intensity value. For this simulation, the external quantum efficiency was $\eta_{ext} = 1$ and $\alpha_b(0) = 1 \times 10^{-3}\ cm^{-1}$.

reduces the heatload from impurities relative to the cooling from Yb^{3+} ions, provided $I_b < I_c$. On the other hand, at wavelengths less than ~1 μm, at small detunings close to the absorption resonances of Yb^{3+}, the saturation intensity of the coolant ions eventually drops below that of the background ($I_c < I_b$). The result is a heightened heatload and reduced cooling efficiency at short wavelengths. Between these opposing limits there exists an intersection of saturation intensity curves versus wavelength (Fig. 2) on the low energy side of the Yb^{3+} resonance. While less obvious in Fig. 3, the same intersection takes place for curves of cooling efficiency at approximately 1010 nm. This intersection point identifies a wavelength λ_{cr} at which the saturation intensities (as well as the cooling efficiencies) of coolant and background ions are equal ($I_b = I_c$).

It is important to recognize that cooling efficiency is independent of intensity at the intersection point. This requires that the saturation intensities of coolant and background ion be equal at λ_{cr}, or that $I_b = I_r(\lambda_{cr})$. At this point the saturation intensity of the background can be determined even when the nature or properties of the background impurities are unknown. Consequently the saturation intensity of background impurities may be determined by simply inserting λ_{cr} into Eq. (2) to find $I_b = I_r(\lambda_{cr})$.

2.2. Impurity saturation in radiation-balanced lasers

Radiation-balanced laser theory developed by Bowman [5] assumed that parasitic heating due to background impurities can generally be neglected and is intensity-independent. This seems reasonable at first because the large thermal load anticipated from near-resonant absorption by the active ions dwarfs that from low concentration impurities. Yet even weak background absorption is still a key limitation to self-cooling in RBLs. Consequently, efforts have been made to include parasitic heating in the RBL heat equation [6,7]. Unfortunately these inclusions were found to eliminate theoretical solutions for radiation-balance in well-characterized RBL materials [17,18]. As summarized in this section, and derived in detail in the Appendices, this problem originates from the neglect of saturation effects at the elevated light intensities that circulate inside RBL lasers. RBL pump fields need to saturate the absorption of active ions to achieve radiation balance. However if the background absorption does not saturate, a linear increase in heat load from impurities accompanies any increase in pump intensity above threshold and radiation balance will be predicted only for unrealistically pure media or extreme pump powers. Inclusion of impurity saturation on the other hand restores solutions for radiation-balance in relatively impure materials and places predictions for RBL operation on a quantitative footing.

Our analysis couples solutions of the population dynamics for saturable active ions and impurities with the heat balance expression, following the approach of Ref. 5 (See Appendix A for details). Solutions for populations N_1 and N_2 of the active ions and N_1' and N_2' of the background impurities that are sustained at pump intensity I_p and laser intensity I_l are substituted into the expression for net thermal power density H in the laser medium. H takes into account net heating by the pump and laser fields, radiative loss, and heating due to impurity absorption, and is given by

$$H = I_p\left[\sigma_{a,p}N_1 - \sigma_{e,p}N_2\right] + I_l\left[\sigma_{a,l}N_1 - \sigma_{a,l}N_2\right] - \eta_e\frac{hc}{\lambda_f}\frac{N_2}{\tau_r} + I_p\left[\sigma'_{a,p}N'_1 - \sigma'_{e,p}N'_2\right] + I_l\left[\sigma'_{a,l}N'_1 - \sigma'_{e,l}N'_2\right] \quad (3)$$

Here $\sigma_{a,i}$ and $\sigma_{e,i}$ are effective absorption and emission cross sections at the pump ($i = p$) and laser ($i = l$) wavelengths respectively. τ_r is the radiative lifetime of the active ion. Background impurities are assumed to form their own 2-level system with effective absorption and emission cross sections $\sigma'_{a,i}$ and $\sigma'_{a,i}$. The first two terms in Eq. (3) account for

energy exchange between the active ions and two cavity modes. The third term quantifies the flow of energy out of the laser medium via fluorescent emission, corrected for escape efficiency. The last two terms are the power absorbed by background impurities at the pump and laser wavelengths.

The radiation-balance condition is obtained by setting the thermal power density in the medium equal to zero ($H=0$). In its original form [5], the radiation-balance condition is written

$$\frac{I_{p,min}}{I_p}+\frac{I_{l,min}}{I_l}=1 \tag{4}$$

where $I_{p,min}$ and $I_{l,min}$ are saturation parameters for the pump and laser fields. This relation specifies the pump and laser mode intensities that are required to balance internal heating with laser cooling. However it does not include saturation of the background impurities unless the saturation parameters in Eq. (4) are re-defined as follows:

$$I_{p,min}=I_{sat,p}\frac{\beta_{pl}}{\beta_p}\frac{\lambda_p}{\lambda_f}\frac{\eta_e\eta_{QE}\lambda_l-\lambda_f(1+R_l)}{\lambda_l-\lambda_p} \tag{5}$$

$$I_{l,min}=I_{sat,l}\frac{\beta_{pl}}{\beta_l}\frac{\lambda_l}{\lambda_f}\frac{\eta_e\eta_{QE}\lambda_p-\lambda_f(1+R_p)}{\lambda_l-\lambda_p} \tag{6}$$

$$R_i=\frac{\sigma' N'_T}{\sigma_{a,i}N_T}\frac{1+\frac{I_p}{I_{sat,p}}+\frac{I_l}{I_{sat,l}}}{1+\frac{I_p}{I'_{sat,p}}+\frac{I_l}{I'_{sat,l}}} \tag{7}$$

$$C=\frac{\beta'_p-\beta'_l}{\beta_p-\beta_l}\frac{\sigma'_{a,p}N'_T}{\sigma_{a,p}N_T}\frac{\beta_p I_{sat,l}}{\beta'_p I'_{sat,l}}\frac{1+\frac{I_p}{I_{sat,p}}+\frac{I_l}{I_{sat,l}}}{1+\frac{I_p}{I'_{sat,p}}+\frac{I_l}{I'_{sat,l}}} \tag{8}$$

Then the radiation balanced condition is

$$\frac{I_{p,min}}{I_p}+\frac{I_{l,min}}{I_l}=1+C \tag{9}$$

When formulated to take into account background saturation, the radiation-balance condition acquires intensity-dependent factors C and R_i. The factor C is negligible ($C\approx 0$) when background saturation intensity is only weakly wavelength-dependent. The factor R_i depends on the small signal absorption coefficients, the pump and laser intensities, and the corresponding saturation intensities. When the saturation intensity of active ions is comparable to the saturation intensity of impurities, the factor R is mainly determined by the ratio of small signal absorption coefficients of the background and coolant ions. If the impurity concentration is considered negligible, or impurities are simply ignored, R vanishes. Eq. (9) then reproduces the prior result of Ref. 5. However when impurities are not ignored, the factor R introduces important dependences on concentration and intensity as shown next.

Fig. 4 plots the radiation-balance condition for 3% Yb:YAG [19] for different values of background absorption with an assumed impurity saturation intensity of $2\times10^4\ W/cm^2$. Note that the curve depicting the radiation-balance condition shifts downward as impurity concentration increases, making it possible to balance the thermal load with background absorption as high as $2\times10^{-3}\ cm^{-1}$ at relatively low pump intensity. Furthermore, when the background absorption falls below $2\times10^{-4}\ cm^{-1}$ the parasitic heating has an insignificant effect on radiation-balance in the model. This explains why the original RBL model that excluded background absorption altogether appeared to fit experimental measurements [17]. By incorporating saturation of both the impurity and coolant ions, the present analysis offers not only a more general model of cooling efficiency but also extends it to impure gain media that previously required unrealistically high powers to operate or that had no analytic solution for radiation-balance at all. Moreover this model indicates that some gain media that fail to achieve any refrigeration in low intensity laser cooling experiments could operate as radiation-balanced lasers. Experimental results showing that background saturation improves cooling efficiency in agreement with this conclusion are covered in Section 3.

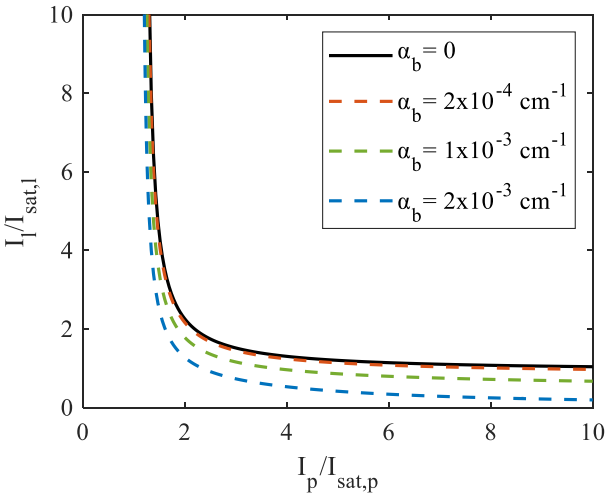

Fig. 4. The theoretical radiation-balance condition plotted for different levels of background absorption. Saturation of parasitic heating shifts the radiation-balance condition down as the background absorption coefficient increases. Fixed parameters for wavelength of the pump, and its absorption and emission cross sections were 1029.3 nm, $1.26\times10^{-21}\ cm^2$ and $2.24\times10^{-20}\ cm^2$ respectively. The wavelength, and absorption and emission cross sections of the laser were 1048 nm, $8.83\times10^{-23}\ cm^2$, and $3.68\times10^{-21}\ cm^2$. The fluorescence lifetime was set to 0.95 ms. Pump and laser saturation intensities were assumed to be $8.59\times10^3\ W/cm^2$ and $5.30\times10^4\ W/cm^2$.

3. Experiments and results

Two different methods were used to determine laser cooling efficiencies experimentally. The first was Differential Luminescence Thermometry (DLT) which is based on emission spectroscopy. The second was Thermal Lens Spectroscopy (TLS) which senses temperature changes via induced refractive index variations. The sample consisted of a 10% Yb^{3+}:$LiYF_4$ crystal of dimensions $3.4\times5.1\times5.6$ mm^3 supported in air on an aerogel disk. The disk (Classic Silica Disk, Aerogel Technologies) assured minimal thermal conduction between the sample and the support, with some degradation being noted over half a year caused by laboratory humidity. Optical excitation was provided by a tunable, single-mode Ti:Al_2O_3 laser (M-squared SolsTiS 5000 PSX-XL). Intensity at the sample in both the DLT and TLS experiments was varied by inserting lenses of different focal lengths into the setup and imaging the focal spots on a beam profiler camera (Thorlabs BC106N-VIS). Once the pump beam was introduced to the sample, a temperature change was recorded by the DLT or TLS method. This observation was then analyzed to compute cooling efficiency by the method described next (Sec. 3.1). Measurements of the effective absorption cross section $\sigma_a(\lambda)$ were made with a SHIMADZU UV-3600 spectrophotometer corrected for instrument response.

3.1. Differential luminescence thermometry

Variations of emission spectra with temperature provide a method of deducing sample temperature by differential luminescence thermometry [3]. In our approach, luminescence was collected with a multimode optical fiber (Ocean Optics QP600-2-VIS-NIR; NA = 0.4) and analyzed with a 0.25 m grating spectrometer (Oriel 74100) equipped with a CCD detector (Andor DU491A-1.7). The sample spectrum recorded at 40 °C served as a reference. Differences between the reference and any chosen luminescence spectrum were integrated over a selected wavelength range to yield the DLT signal. These signals were then calibrated by varying the sample temperature from 40 °C to 10 °C in steps of 0.5 °C in a temperature-controlled oven (Quantum Northwest Flash 300) with an accuracy of ±0.01 K. As in earlier work [19], temperatures determined by DLT agreed with crystal surface temperatures obtained using a thermal camera (FLIR A655sc) within the stated accuracy. The acquisition time of DLT measurements was 2 s, so it was possible to follow cooling or heating dynamics in real time. This is illustrated in Figs. 5 and 6 where DLT signals acquired at 1015 nm and 920 nm show representative cooling and heating curves at long and short wavelengths in the experimental range respectively.

Time-dependent temperature changes can be analyzed to determine cooling efficiency directly from the thermal balance equation for the sample (Eq. (10)). This equation [20,21] accounts for the various contributions to heating power in a crystal of temperature T, emissivity ε and surface area A_{surf} under the assumption that it is enclosed by a blackbody radiator at the environmental temperature T_0.

$$cM\frac{dT}{dt} = -\eta_c P_{abs} + A_{surf}\varepsilon\sigma_B\left(T_0^4 - T^4\right) + \left(h_{cv}A_{surf} + k\frac{A_{ct}}{L}\right)(T_0 - T) \qquad (10)$$

The parameters σ_B h_{cv}, k, A_{ct}, and L in Eq. (10) are the Stefan-Boltzmann constant, convective heat transfer coefficient, thermal conductivity of the link, cross-sectional area, and sample length, respectively. Other constants of the 10% Yb^{3+}:$YLiF_4$ sample included specific heat c = 0.79 J/g·K [22] and mass (M = 0.408 g) determined using a precision balance (QUINTEX213-1S).

The left hand side of Eq. (10) is determined directly by observed rates of temperature change, together with some fixed sample properties. The rate of heating or cooling then reflects the balance of energy loss or gain processes from the three terms on the right side of the equation. These terms describe in succession the laser-induced energy gain or loss per unit time, the power exchanged between the sample and its surroundings due to blackbody radiation, and the power lost or gained through thermal conduction. The conduction term has two parts, corresponding to contact of the sample surface with air and conduction through the sample support. The second and third terms of the equation depend on how different the sample and environmental temperatures are. For small excursions in temperature the difference between T and T_0 is small. For this reason the second and third terms of Eq. (10) can be neglected when temperature changes are small or times are short. Thermal balance in the crystal is then determined solely by the laser cooling term containing the cooling efficiency η_c. At short times, the cooling rate is linear in time as seen in Figs. 5 and 6 and is equal to the cooling power. A simple determination of η_c therefore becomes possible from observations of temperature change at short times using

$$\eta_c = P_{abs}^{-1} cM dT/dt \qquad (11)$$

when the absorbed power is known from careful measurements of the incident, reflected, and transmitted pump power.

For large excursions of temperature from ambient (or at long times), the temperature T differs significantly from T_0. Its dependence on time therefore becomes nonlinear and Eq. (11) ceases to be a valid approximation. In practice it was found that excellent linear fits were obtained for temperature excursions of ΔT<1 K or for times less than 1 min. Consequently, restriction of data analysis to these conditions furnished simple but accurate determinations of the cooling efficiency at arbitrary wavelengths.

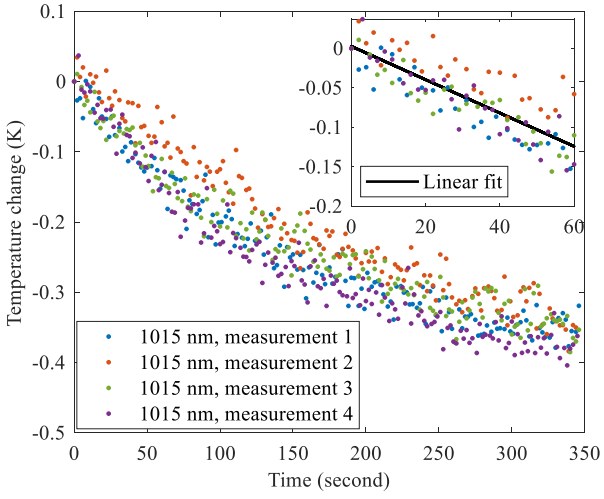

Fig. 5. Temperature change versus time in Yb^{3+}:$LiYF_4$ recorded by DLT at a pump power of 0.8 W and a wavelength of λ = 1015 nm in the cooling range. The inset shows that during the first 60 s the temperature decrease is well described by a linear regression with a slope of $-2.11\times10^{-3} K/s$.

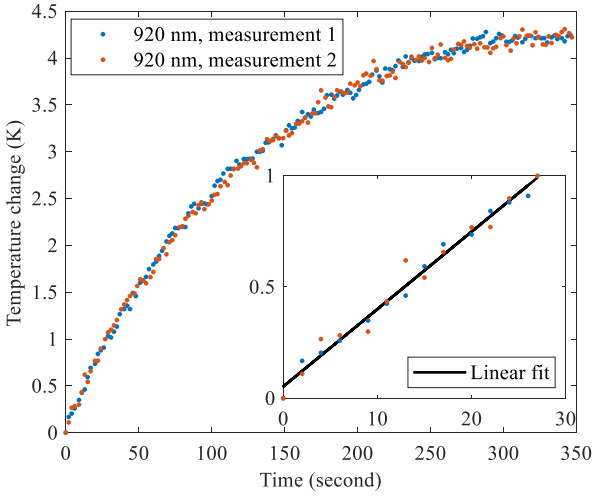

Fig. 6. Temperature change versus time in Yb^{3+}:$LiYF_4$ recorded by DLT at a pump power of 0.8 W and a wavelength of λ = 920 nm in the heating range. The inset shows that during the first 30 s while the temperature changed by ΔT = 1 K the temperature increase was well described by a linear regression with a slope of $3.48\times10^{-2} K/s$.

3.2. Thermal lens spectroscopy

Thermal lens spectroscopy was used to probe variations of refractive index induced by light from a tunable, single-mode Ti:Al_2O_3 laser. The incident beam was chopped mechanically to enable synchronous detection and thermal lens signals generally exhibited two components. One was a relatively fast transient arising from population transfer. Transitions between ground and excited states change the refractive index because excited state polarizability is generally greater than the ground state polarizability. The other component was a slower transient arising from thermal diffusion which changes the index through its temperature dependence. Both components must be included for accurate modeling [19,23,24]. A He–Ne probe laser which propagated

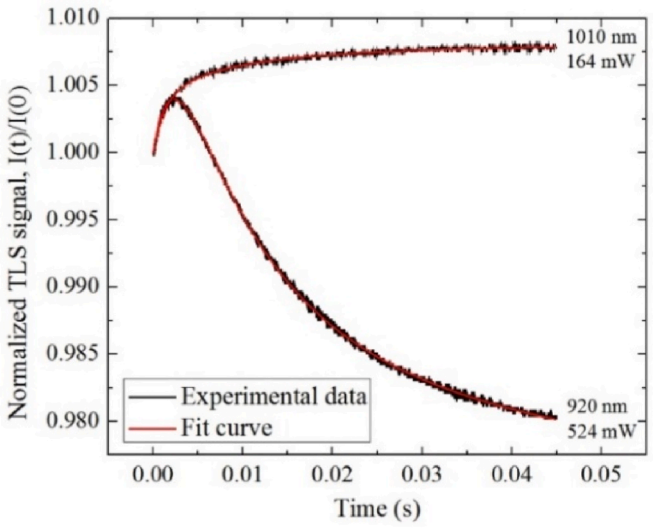

Fig. 7. Normalized signals obtained by thermal lens spectroscopy versus time at 1010 nm and 920 nm, illustrating cooling and heating in 10% Yb^{3+}:$LiYF_4$. Best fit curves are shown in red.

counter to the pump beam was transmitted through a 2 mm pinhole to sense index changes by monitoring the intensity variations from thermal lensing with a photodiode. TLS signals were then normalized and fitted with the theory of Ref. 24 to account for population and thermal effects. Examples of TLS data and fits at two wavelengths are displayed in Fig. 7. Best fits to the data yielded the thermal lens strength from which the cooling efficiency η_c is derived.

3.3. Results and analysis

Figs. 8 and 9 present plots of cooling efficiencies as a function of wavelength, measured with TLS and DLT at several intensities. The pump intensities and beam radii corresponding to these measurements are tabulated in Table 1. In both figures note that the slopes of the

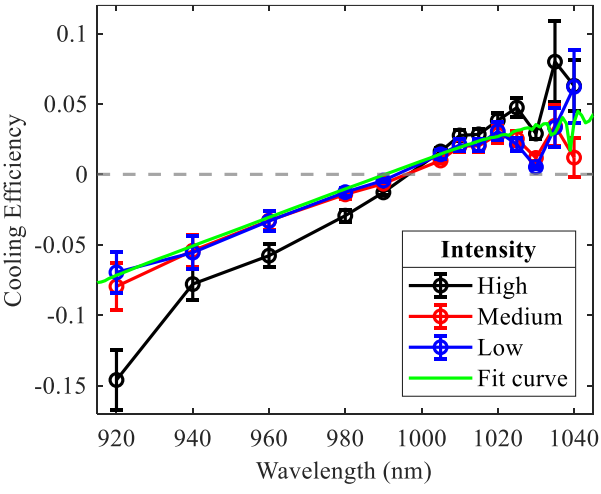

Fig. 8. TLS measurements of experimental cooling efficiencies versus wavelength at three intensities. The intensities correspond to the listings in Table 1 and were produced by focusing powers in the range 50–540 mW to the tabulated spot sizes. A host parameter of $\Theta = 1.4\ W^{-1}$ was assumed for all three data sets. The external quantum efficiency and background absorption coefficient determined by the fit to low intensity data (green) were $\eta_{ext} = 1.01 \pm 0.02$ and $\alpha_b(0) = (5 \pm 2) \times 10^{-4}\ cm^{-1}$.

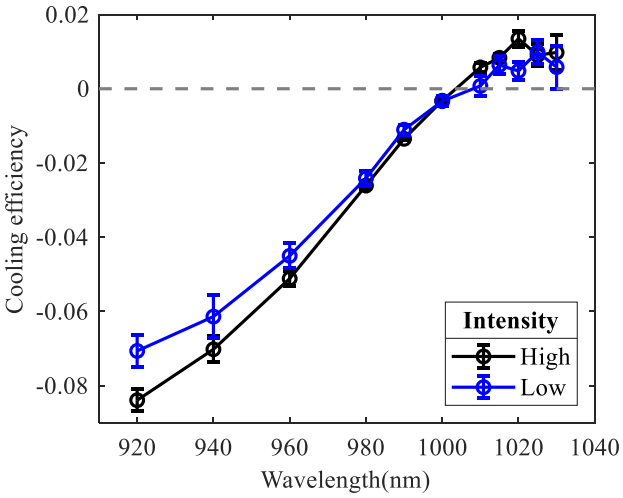

Fig. 9. DLT measurements of cooling efficiencies in 10% Yb^{3+}:$LiYF_4$ as a function of wavelength and intensity. All measurements were taken with a pump power of 0.8 W. High and low intensities were reached by varying beam size according to Table 1.

Table 1
Pump beam radius (half width at $1/e^2$ intensity) and intensity values used for the measurements presented in Figs. 8 and 9. Entries indicate the small variations of intensity at multiple wavelengths for each intensity category.

	Beam radius (μm)	Intensity (W/cm^2)
DLT High	32.4–39.3	$(1.6 - 2.4) \times 10^4$
DLT Low	284–318	$(2.0 - 3.3) \times 10^2$
TLS High	38.0–52.5	$(2.3 - 4.4) \times 10^3$
TLS Medium	65–103	$(0.6 - 1.2) \times 10^3$
TLS Low	121–145	$(3 - 4.4) \times 10^2$

cooling efficiency curves steepen with increasing intensity. At long wavelengths the cooling efficiencies at elevated intensities also exceed those at low intensity. This behavior is the main result of the current paper [25]. Intensity-dependent improvement in η_c implies that the saturation of coolant and impurity ions is different and varies with wavelength. This effect, which we refer to as differential absorption saturation can be explained by the arguments of Section 2.1.

A further thing to note in Figs. 8 and 9 is that the experimental traces for efficiency at different intensities intersect around 1000 nm. At this wavelength the curves all pass through a common point as predicted by the theory of Sec. 2. The significance of this is that cooling efficiency is the same for all intensities, or that the cooling efficiency is independent of intensity there. For this to be the case, the saturation intensity of background impurities must equal that of the coolant ions, computed from Eq. (2) to be $\sim 2.6 \times 10^4\ W/cm^2$. Hence a determination of the wavelength (λ_{cr}) at which the crossing takes place permits one to deduce the saturation intensity of background impurity absorption which is the key limitation to cooling efficiency.

Data taken in the cooling range at wavelengths longer than $\lambda_{cr} = 1000$ nm in both figures show the same crossing wavelength and heightened cooling efficiencies at elevated intensities. This is consistent with an increase of the Yb^{3+} saturation intensity relative to the background as the detuning from the Yb^{3+} absorption peak increases. In this range ($\lambda > \lambda_{cr}$) the observations can be explained by low background saturation intensity ($I_b(\lambda) < I_r(\lambda)$), which leads to reduced parasitic heating and heightened efficiency. Data taken in the heating range at slightly shorter wavelengths ($\lambda < \lambda_{cr}$) have progressively smaller detunings from the Yb^{3+} absorption peak. Cooling efficiencies drop but still display an intensity dependence, consistent with a reduction of the Yb^{3+}

saturation intensity near resonance.

In Figs. 8 and 9 the experimental traces between 960 nm and 920 nm diverge more than the theoretical curves in Fig. 3. This may be attributable to a large excited state population of Yb^{3+} ions close to resonance where saturation is prevalent. A high occupation of the upper state can enhance energy transfer and non-radiative processes between Yb^{3+} and other rare earth impurities [26,27]. Indeed, characteristic green upconversion emission from Er^{3+} ions was visible to the eye at these wavelengths, highlighting the onset of a small heatload not taken into account in the theory of Section 2. Apart from this minor effect in the 920–960 nm range, there was no evidence that trace amounts of Er^{3+} contributed significantly to cooling dynamics at wavelengths longer than 1 μm where this ion has no ground state absorption transitions.

4. Discussion

TLS and DLT measurements in 10% Yb^{3+}:$LiYF_4$ were in good mutual agreement. Both sets of experiments revealed an intensity dependence of laser cooling and efficiency enhancement at elevated laser intensities. These effects are in accord with differential absorption saturation theory (Sec. 2 and Appendices) which predicts that saturation of the background absorption at high pump intensities can increase laser cooling efficiency (provided that $I_b < I_r$). The observation of a crossing point (λ_{cr}) in efficiency curves measured at different intensities furnishes a new method of determining the saturation intensity of background absorption, applicable even when the absorbing species is not identified. The experimental value for our sample was found to be $I_b = I_r(\lambda_{cr}) = 2.6\times 10^4$ W/cm^2 by inserting the observed wavelength λ_{cr} together with measured cross sections into Eq. (1).

The background saturation intensity I_b is surprisingly low. This result may stem from the valence and site symmetry of the dominant impurity. Divalent iron is thought to be the main source of background absorption in Yb:$LiYF_4$ crystals [10], but this impurity could also substitute at Yttrium (Y^{3+}) sites in $LiYF_4$, rendering it trivalent. If this were the case, we note that trivalent iron in a material like Fe:YAG has a low-energy transition from $^6A_{1g}$ to $^4T_{1g}$ that is both spin- and parity-forbidden [29]. It is known that there is a long-lived excited state accessed by this forbidden transition with a fluorescence lifetime of 170 μs [30], making it easy to saturate. In the YAG host the transition is centered at 903 nm and is broad enough that it has an absorption cross section of $\sigma_a = 1.2 \times 10^{-20}$ cm^2 at 1000 nm [16]. While the emission cross section in YAG and both the absorption and emission cross sections in $LiYF_4$ are unknown, it is not unreasonable to surmise that the background saturation intensity of trivalent iron could be extremely low at this wavelength in $LiYF_4$. Basing an estimate solely on σ_a of Fe^{3+}:YAG, the calculated saturation intensity of trivalent iron would be 9.9×10^4 W/cm^2, which is 23% lower than that of Yb^{3+} at 1000 nm calculated in the same way. This agrees roughly with the saturation intensity I_b determined for the background in our sample, as well as the requirement that $I_b < I_r$ for enhanced cooling (albeit in a different host). Much higher saturation intensities would be expected for other valences like Fe^{2+} or Fe^{4+} since transitions near 1000 nm are allowed and originate from short-lived upper states [31]. Fe^{2+} and Fe^{4+} would not saturate at the low intensities of our experiments. However a sizeable proportion of Fe^{3+} ions could easily saturate and become less absorptive, thereby causing an improvement of cooling efficiency. Consequently, we consider Fe^{3+} to be a viable candidate for the saturable background species in our experiments.

Impurities other than iron could of course contribute significantly to background absorption in crystalline Yb^{3+}:$LiYF_4$. Earlier work found significant correlations between background absorption levels and elements such as vanadium and chromium [10]. In certain valence states these elements could have low saturation intensities near 1000 nm Cr^{4+} ions in YAG for example have a saturation intensity that is only 10% of that of Yb^{3+} at 1000 nm [32]. Consequently a mixture of background absorption species might be involved in the reduction of parasitic heating and enhanced cooling reported here at high pump intensities. Although we are unable to state with certainty what ionic species causes intensity-dependent laser cooling, it does seem that transition metal and other impurities present as trace elements have properties consistent with the experimentally-determined saturation intensity $I_b = 2.6 \times 10^4$ W/cm^2.

Our results show that the major efforts that have been made in the past to purify optical refrigerants are not the only way to improve cooling efficiency or to reach lower temperatures in a given material. In Appendix B, optical saturation is shown to offer a possible route for reaching lower minimum achievable temperatures (MATs). The achievement of lower temperatures would significantly improve the performance of imaging arrays by reducing electronic noise. We note however that because absorption coefficients are temperature-dependent [28], characterization of optical saturation at low temperatures will be necessary to predict precisely how successful this cooling strategy may be in practice. Only if the background absorption saturates before that of the coolant ions in the cryogenic range ($I_b < I_r$) will MATs drop as the result of operation at high pump intensities (see Fig. B1).

The inclusion of background saturation in laser cooling analysis not only reveals that optical refrigeration can be improved at high intensities, but makes an important correction to radiation-balanced laser theory. When background saturation is included, stable solutions for radiation balance are found at impurity absorption levels typical of batch processed crystals ($\alpha_b(0) > 10^{-4}\ cm^{-1}$) rather than in ultrapure ($\alpha_b(0) < 10^{-4}\ cm^{-1}$) laser media exclusively (Fig. 4 and Appendix A). More accurate predictions and modeling are enabled when parasitic heating and background saturation are included in the heat equation of RBLs. This finding will therefore promote the use of cooling materials that are not well developed and currently suffer from higher background impurity levels, such as KYW [19]. That is, this research opens an avenue for laser refrigeration of impure materials that could not be cooled previously at all.

5. Conclusions

Steady-state analysis of ASF laser cooling has been presented that predicts improved cooling efficiency at elevated pump intensities whenever the saturation intensity of background absorption is less than that of the coolant ions. Experimentally, this prediction was realized in 10% Yb^{3+}:$LiYF_4$ at wavelengths longer than 1000 nm. DLT and TLS measurements showed that the cooling efficiency doubled with increased pump intensity near 1035 nm, a phenomenon ascribed to low saturation intensity of the dominant impurity, thought to be trivalent iron. A novel method was devised to measure the saturation intensities of background and coolant ions that confirmed an unexpectedly low value of background saturation intensity in the range of this wavelength. Thus saturation accounted for the intensity-dependent cooling efficiencies observed in this work, consistent with the new analysis. A further conclusion can be drawn that in self-cooled lasers, which operate with very high circulating pump intensity, improved cooling efficiency from saturation effects will permit the attainment of radiation balance at pump intensities lower than expected from prior analysis. The results and model developed here also predict that stable RBL operation should

be achievable in relatively impure laser materials, including some that do not even show net cooling at low intensities. Hence this finding improves the prospects for RBLs in a much wider variety of laser hosts and at lower pump intensities than previously thought possible.

An original method was introduced to determine the saturation intensity of background absorption in a 10% Yb^{3+}: $LiYF_4$ crystal. The technique makes use of systematic measurements of laser cooling efficiency by Differential Luminescence Thermometry (DLT) and Thermal Lens Spectroscopy (TLS) as a function of wavelength and incident intensity. Results revealed a wavelength at which all cooling efficiency curves intersected, regardless of intensity. The crossing point observed at $\lambda_{cr} = 1000$ nm in 10% Yb^{3+}: $LiYF_4$ indicated that the cooling efficiencies were independent of intensity at this wavelength. Consequently the saturation intensity of Yb^{3+} which varied strongly with detuning from resonance had to be equal to the saturation intensity of the background species there. This meant that the background saturation intensity could be computed from the analytic expression for the coolant ions at the unique wavelength λ_{cr} (yielding $I_b = I_r(\lambda_{cr}) = 2.6 \times 10^4$ W/cm^2). For $\lambda > \lambda_{cr}$, higher pump intensities improved the cooling efficiency significantly. These findings agreed well with the differential saturation model incorporating intensity-dependent coolant ion and background absorption.

CRediT authorship contribution statement

Long Cheng: Conceptualization, Methodology, Investigation, Formal analysis, Writing – original draft, Writing – review & editing. **Laura B. Andre:** Conceptualization, Methodology, Investigation. **Gabriela L. Almeida:** Investigation. **Luis H.C. Andrade:** Supervision, Investigation. **Sandro M. Lima:** Supervision, Investigation. **Junior R. Silva:** Funding acquisition, Supervision, Methodology, Investigation, Resources. **Tomaz Catunda:** Methodology, Validation. **Yannick Guyot:** Resources. **Stephen C. Rand:** Project administration, Conceptualization, Writing – original draft, Writing – review & editing, Funding acquisition.

Declaration of competing interest

The authors declare that they have no known competing financial interests or personal relationships that could have appeared to influence the work reported in this paper.

Acknowledgments

The authors would like to thank Zackery L. Thune and Professor Thomas R. Bieler of Michigan State University for the X-ray diffraction measurements.

This work was supported by the Air Force Office of Scientific Research [MURI FA9550-16-0383] and Conselho Nacional de Desenvolvimento Científico e Tecnológico [305067/2019-2 (S.M.L.), 306452/2018-9 (L.H.C.A.), 425930/2018-1, 310772/2019-2 (J.R.S.)].

APPENDIX A

Analysis of Radiation-Balanced Lasing with Saturable Impurity Absorption

The active ions of a radiation-balanced laser (RBL) have previously been analyzed as 2-level systems [17]. Here we extend such an analysis to include background impurity ions as 2-level systems. The condition for operating a laser under radiation-balanced conditions is evaluated taking optical saturation of both species into account.

The ground and excited state densities (population per unit volume) of the active ions and background impurities are denoted by N_1, N_2 and N_1', N_2' respectively. Their total densities are therefore given by the sums

$$N_T = N_1 + N_2 \tag{A.1}$$

$$N_T' = N_1' + N_2' \tag{A.2}$$

The rate equation for upper state population of the active ion is

$$\frac{dN_2}{dt} = \frac{I_p \lambda_p}{hc} \cdot \left[\sigma_a(\lambda_p, T) N_1 - \sigma_e(\lambda_p, T) N_2\right] + \frac{I_l \lambda_l}{hc} \cdot \left[\sigma_a(\lambda_l, T) N_1 - \sigma_e(\lambda_l, T) N_2\right] - \frac{N_2}{\tau_r} - \gamma_{nr} N_2 \tag{A.3}$$

where σ_a and σ_e are effective absorption and emission cross sections which can be measured directly. These effective cross sections include effects of the Boltzmann distribution and are therefore temperature dependent. I_p and I_l denote pump (p) and laser (l) intensities at wavelengths of λ_p and λ_l. τ_r is the radiative lifetime of the active ion. By introducing the fluorescence lifetime τ_f which is the inverse sum of the radiative and non-radiative decay rates γ_r and γ_{nr}, the rate equation for the active ion simplifies to:

$$\frac{dN_2}{dt} = \frac{I_p \lambda_p}{hc} \cdot \left[\sigma_{a,p} N_1 - \sigma_{e,p} N_2\right] + \frac{I_l \lambda_l}{hc} \cdot \left[\sigma_{a,l} N_1 - \sigma_{a,l} N_2\right] - \frac{N_2}{\tau_f} \tag{A.4}$$

For the background impurities the corresponding equation is

$$\frac{dN_2'}{dt} = \frac{I_p \lambda_p}{hc} \cdot \left[\sigma_{a,p}' N_1' - \sigma_{e,p}' N_2'\right] + \frac{I_l \lambda_l}{hc} \cdot \left[\sigma_{a,l}' N_1' - \sigma_{e,l}' N_2'\right] - \frac{N_2'}{\tau'} \tag{A.5}$$

The internal quantum efficiency of the active ion is given by the usual ratio

$$\eta_{QE} = \frac{\tau_f}{\tau_r} \tag{A.6}$$

The net thermal power density H deposited in the medium by incident or internal light fields includes the power per unit volume absorbed from the pump and internal laser fields as well as that released by radiative and non-radiative relaxation processes. In the calculation of H, the escape efficiency η_e of active ion fluorescence is taken into account and background impurities are presumed to contribute only via absorption.

$$H = I_p\left[\sigma_{a,p}N_1 - \sigma_{e,p}N_2\right] + I_l\left[\sigma_{a,l}N_1 - \sigma_{a,l}N_2\right] - \eta_e\frac{hc}{\lambda_f}\frac{N_2}{\tau_r} + I_p\left[\sigma'_{a,p}N'_1 - \sigma'_{e,p}N'_2\right] + I_l\left[\sigma'_{a,l}N'_1 - \sigma'_{e,l}N'_2\right] \tag{A.7}$$

Under steady-state conditions the level populations have no time dependence. By solving Eq. (A.4) in this limit, the population differences at the pump and laser wavelengths are found to be

$$\Delta N_{p,ss} = N_1 - \frac{\sigma_{e,p}}{\sigma_{a,p}}N_2 = N_T\frac{\frac{\beta_l I_l}{\beta_{pl} I_{sat,l}} + 1}{\frac{I_p}{I_{sat,p}} + \frac{I_l}{I_{sat,l}} + 1} \tag{A.8}$$

$$\Delta N_{l,ss} = N_1 - \frac{\sigma_{e,l}}{\sigma_{a,l}}N_2 = N_T\frac{-\frac{\beta_p I_p}{\beta_{pl} I_{sat,p}} + 1}{\frac{I_p}{I_{sat,p}} + \frac{I_l}{I_{sat,l}} + 1} \tag{A.9}$$

in terms of corresponding saturation intensities defined by

$$I_{sat,p} \equiv \frac{hc}{\lambda_p\tau_f\left[\sigma_{a,p} + \sigma_{e,p}\right]} \tag{A.10}$$

and

$$I_{sat,l} \equiv \frac{hc}{\lambda_l\tau_f\left[\sigma_{a,l} + \sigma_{e,l}\right]} \tag{A.11}$$

In Eqs. (A.8-A.11) additional parameters have been introduced in the form

$$\beta_i \equiv \frac{\sigma_{a,i}}{\sigma_{a,i} + \sigma_{e,i}} \tag{A.12}$$

where i=(l,p), and

$$\beta_{pl} \equiv \frac{\beta_p\beta_l}{\beta_p - \beta_l} \tag{A.13}$$

The population difference of the impurity ions at the pump wavelength is similarly determined by solving Eq. (A.5) in steady-state. The result is

$$\Delta N'_{p,SS} = N'_1 - \frac{\sigma'_{e,p}}{\sigma'_{a,p}}N'_2 = N'_T\frac{\frac{\beta'_l I_l}{\beta'_{pl} I'_{sat,l}} + 1}{1 + \frac{I_p}{I'_{sat,p}} + \frac{I_l}{I'_{sat,l}}} \tag{A.14}$$

$$\Delta N'_{l,SS} = N'_1 - \frac{\sigma'_{e,l}}{\sigma'_{a,l}}N'_2 = N'_T\frac{-\frac{\beta'_p I_p}{\beta'_{pl} I'_{sat,p}} + 1}{1 + \frac{I_p}{I'_{sat,p}} + \frac{I_l}{I'_{sat,l}}} \tag{A.15}$$

where

$$\beta'_i \equiv \frac{\sigma'_{a,i}}{\sigma'_{a,i} + \sigma'_{e,i}} \tag{A.16}$$

$$\beta'_{pl} \equiv \frac{\beta'_p\beta'_l}{\beta'_p - \beta'_l} \tag{A.17}$$

and

$$I'_{sat,i} = \frac{hc}{\lambda_i\tau'\left[\sigma'_{a,i} + \sigma'_{e,i}\right]}\cdot(\mathrm{i} = \mathrm{l}, \mathrm{p}) \tag{A.18}$$

The heat equation can now be written in a form that accounts for saturation effects and non-radiative decay in the laser medium.

$$\mathrm{H} = I_p\left[\sigma_{a,p}\Delta N_p + \sigma'_{a,p}\Delta N'_p\right]\left[1-\eta_{ext}\eta_{abs,p}\frac{\lambda_p}{\lambda_f}\right] + I_l\left[\sigma_{a,l}\Delta N_l + \sigma'_{a,l}\Delta N'_l\right]\left[1-\eta_{ext}\eta_{abs,l}\frac{\lambda_l}{\lambda_f}\right] \tag{A.19}$$

The external quantum efficiency is the product of the internal value and the escape efficiency ($\eta_{ext} = \eta_e\eta_{QE}$). In Eq. (A.19) absorption efficiencies have been defined for the pump and laser fields according to

$$\eta_{abs,p} = \frac{\sigma_{a,p}\Delta N_p}{\sigma_{a,p}\Delta N_p + \sigma'_{a,p}\Delta N'_p} \tag{A.20}$$

$$\eta_{abs,l} = \frac{\sigma_{a,l}\Delta N_l}{\sigma_{a,l}\Delta N_l + \sigma'_{a,l}\Delta N'_l} \tag{A.21}$$

Radiation balance is achieved when $H = 0$. For the case of *no background absorption* the heat equation yields

$$I_p\left[\sigma_{a,p}\Delta N_p\right]\left[1-\eta_{ext}\frac{\lambda_p}{\lambda_f}\right] + I_l\left[\sigma_{a,l}\Delta N_l\right]\left[1-\eta_{ext}\frac{\lambda_l}{\lambda_f}\right] = 0 \tag{A.22}$$

From this expression the *condition for radiation balance* can be re-written in the form

$$\frac{I_{p,min}}{I_p} + \frac{I_{l,min}}{I_l} = 1 \tag{A.23}$$

in agreement with Ref. [5]. The intensities in Eq. (A.23) are defined to be

$$I_{p,min} = I_{sat,p}\frac{\beta_{pl}}{\beta_p}\frac{\lambda_p}{\lambda_f}\frac{\eta_{ext}\lambda_l - \lambda_f}{\lambda_l - \lambda_p} \tag{A.24}$$

and

$$I_{l,min} = I_{sat,l}\frac{\beta_{pl}}{\beta_l}\frac{\lambda_l}{\lambda_f}\frac{\eta_{ext}\lambda_p - \lambda_f}{\lambda_l - \lambda_p} \tag{A.25}$$

When saturation of the background absorption is taken into account, the radiation balance condition is altered from that in Eq. (A.23). By modifying the definitions of $I_{p,min}$ and $I_{l,min}$, the radiation balance condition can nevertheless be preserved in a form similar to Eq. (A.23), namely

$$\frac{I_{p,min}}{I_p} + \frac{I_{l,min}}{I_l} = 1 + C \tag{A.26}$$

where

$$C = \frac{\beta'_p - \beta'_l}{\beta_p - \beta_l}\frac{\sigma'_{a,p}N'_T}{\sigma_{a,p}N_T}\frac{\beta_p I_{sat,l}}{\beta'_p I'_{sat,l}}\frac{1+\frac{I_p}{I_{sat,p}}+\frac{I_l}{I_{sat,l}}}{1+\frac{I_p}{I'_{sat,p}}+\frac{I_l}{I'_{sat,l}}} \tag{A.27}$$

$$I_{p,min} = I_{sat,p}\frac{\beta_{pl}}{\beta_p}\frac{\lambda_p}{\lambda_f}\frac{\eta_{ext}\lambda_l - \lambda_f(1+R_l)}{\lambda_l - \lambda_p} \tag{A.28}$$

$$I_{l,min} = I_{sat,l}\frac{\beta_{pl}}{\beta_l}\frac{\lambda_l}{\lambda_f}\frac{\eta_{ext}\lambda_p - \lambda_f\left(1+R_p\right)}{\lambda_l - \lambda_p} \tag{A.29}$$

and

$$R_p = \frac{\sigma' N'_T}{\sigma_{a,p}N_T}\frac{1+\frac{I_p}{I_{sat,p}}+\frac{I_l}{I_{sat,l}}}{1+\frac{I_p}{I'_{sat,p}}+\frac{I_l}{I'_{sat,l}}} \tag{A.30}$$

$$R_l = \frac{\sigma' N'_T}{\sigma_{a,l}N_T}\frac{1+\frac{I_p}{I_{sat,p}}+\frac{I_l}{I_{sat,l}}}{1+\frac{I_p}{I'_{sat,p}}+\frac{I_l}{I'_{sat,l}}} \tag{A.31}$$

If the variation of the impurity cross sections with wavelength is weak ($\beta'_p \approx \beta'_l$), or the effective absorption cross section is larger than the effective emission cross section ($\beta'_i > 0.5$), the factor C is negligible ($C \approx 0$). Under these circumstances, impurity saturation plays an insignificant role in RBL operation and the radiation balance condition (A.26) has exactly the same form as Eq. (A.23), published originally in Ref. 5.

Appendix B

Optical Saturation in Laser Cooling

The effect of optical saturation on laser cooling can readily be evaluated from the expressions of Appendix A by setting the laser intensity equal to zero (i.e. $I_l = 0$ in (A.4), (A.5), and (A.7)). Then the equations can be re-solved for steady-state results with no internal field. The results below then include saturation effects in the expression for cooling power by anti-Stokes fluorescence refrigeration.

For active ions, absent any internal laser field, the rate equation for upper state population is

$$\frac{dN_2}{dt} = \frac{I_p \lambda_p}{hc} \cdot \left[\sigma_a(\lambda_p, T) N_1 - \sigma_e(\lambda_p, T) N_2\right] - \frac{N_2}{\tau_f} \tag{B.1}$$

For the impurities it is

$$\frac{dN_2'}{dt} = \frac{I_p \lambda_p}{hc} \cdot \left[\sigma_{a,p}' N_1' - \sigma_{e,p}' N_2'\right] - \frac{N_2'}{\tau'} \tag{B.2}$$

The heat equation is also simplified, reducing to

$$\mathrm{H} = I_p\left[\sigma_{a,p} N_1 - \sigma_{e,p} N_2\right] - \eta_e \frac{hc}{\lambda_f} \frac{N_2}{\tau_r} + I_p\left[\sigma_{a,p}' N_1' - \sigma_{e,p}' N_2'\right] \tag{B.3}$$

Because there is no internal laser field to consider in single pump beam refrigeration, the population differences for steady illumination are simply

$$\Delta N = \frac{N_T}{\frac{I_p}{I_{sat}} + 1} \tag{B.4}$$

and

$$\Delta N' = \frac{N_T'}{\frac{I_p}{I_{sat}'} + 1} \tag{B.5}$$

Where $I_{sat} = \frac{hc}{\lambda_p \tau_f [\sigma_a(\lambda_p, T) + \sigma_e(\lambda_p, T)]}$ and $I_{sat}' = \frac{hc}{\lambda_p \tau' [\sigma_{a,p}' + \sigma_{e,p}']}$. Under steady-state conditions, the power/volume obtained from the heat equation is

$$\mathrm{H} = I_p\left[\sigma_a(\lambda_p, T)\Delta N + \sigma_{a,p}' \Delta N_p'\right] \cdot \left[1 - \frac{\sigma_a(\lambda_p, T)\Delta N}{\sigma_a(\lambda_p, T)\Delta N + \sigma_{a,p}' \Delta N_p'} \eta_{ext} \frac{\lambda_p}{\lambda_f}\right] \tag{B.6}$$

The final expression for cooling power in the presence of optical saturation of active ions and background impurities is therefore

$$P_{cooling} = -P_{abs}\left[1 - \frac{\sigma_a(\lambda_p, T)\Delta N}{\sigma_a(\lambda_p, T)\Delta N + \sigma_{a,p}' \Delta N_p'} \eta_{ext} \frac{\lambda_p}{\lambda_f}\right] \tag{B.7}$$

The intensity dependence of absorption for cooling ions and impurities theoretically affects the minimum achievable temperature (MAT) in ASF cooling. Phonon sideband absorption is proportional to the average phonon occupation denoted by

$$n(T) = [\exp(\hbar\Omega / k_B T_0) - 1]^{-1} \tag{B.8}$$

Hence temperature dependent absorption coefficient of active ions is

$$\alpha_r(T) = \frac{n(T)}{n(T_0)} \alpha_r(T_0) \tag{B.9}$$

The effect of saturation on MATs can be analyzed by setting the usual expression for cooling efficiency equal to zero and solving for temperature with the approximation $\hbar\Omega = h(\nu_f - \nu) \approx k_B T$. The resulting expression for MAT is

$$T_{\min} = \hbar\Omega \Big/ \left(k_B \log_e \left\{1 + \left(\eta_{ext}\left(\frac{\nu_f}{\nu}\right) - 1\right) \frac{\alpha_r(I)}{\alpha_b(I)} [\exp(\hbar\Omega / k_B T_0) - 1]\right\}\right) \tag{B.10}$$

In the figures below the saturation intensity depends on wavelength and its value is calculated using the Yb^{3+} fluorescence lifetime and cross sections. The background saturation intensity was assigned the experimental value (see text). Room temperature absorption spectra were also used to prepare the plots which illustrate important aspects of saturation behavior. Figure B1 plots values of T_{min} versus assumed ratios of background and coolant ion saturation intensities and versus wavelength in Yb^{3+}:$LiYF_4$. Note that in Fig. B1(a) if $I_b \gg I_r$ the cooling power saturates before the background heating and no benefit is realized at high pump intensities. When $I_b = I_r$ there is no dependence of net cooling on intensity at all. However, if $I_b < I_r$, the MAT drops substantially with increasing pump intensity. Considering only the temperature dependence of phonon sideband absorption in Yb^{3+}:$LiYF_4$, the curves in Figure B1(b) therefore show theoretically that if the ratio of saturation intensities were $I_r/I_b = 1.58$ as in the experiment, the MAT would drop from roughly 120 K–100 K in this material by exploiting saturation.

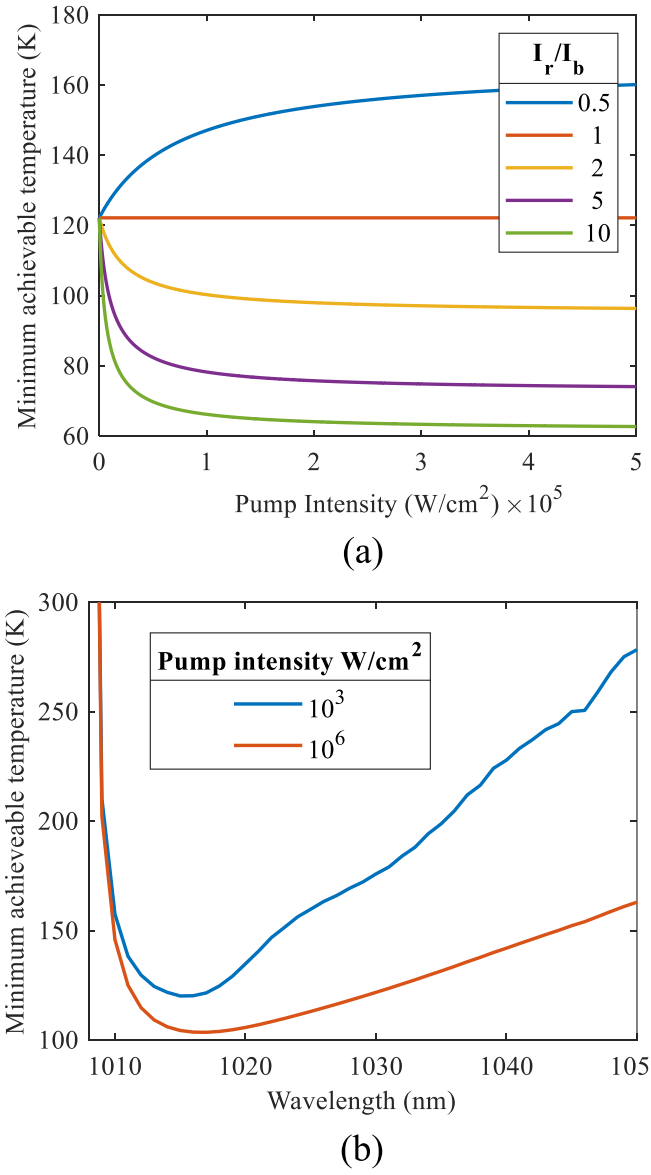

Fig. B.1. (a) Theoretical MAT values at 1017 nm from Eq. (B.10) versus pump intensity for different ratios of coolant to background saturation intensities in 10% Yb^{3+}:$LiYF_4$. The Yb^{3+} saturation intensity was fixed at $I_r = 4.1 \times 10^4$ W/cm^2 (at 1017 nm) and the background value was varied to illustrate different cases. The unsaturated absorption coefficient of coolant ions was 0.296 cm^{-1} at 1017 nm (experimental). (b) Theoretical MAT curves versus wavelength using the experimentally-determined ratio $I_r/I_b = 1.58$ at pump intensities of 10^3 W/cm^2 (blue) and 10^6 W/cm^2 (red). The saturation intensities of Yb^{3+} and background were $I_r = 4.1 \times 10^4$ W/cm^2 (at 1017 nm) and $I_b = 2.6 \times 10^4$ W/cm^2 in the simulation. Mean fluorescence wavelength was $\lambda_{MFW} = 997.6$ nm, external quantum efficiency was taken to be $\eta_{ext} = 0.99$, and the background absorption coefficient was $\alpha_b = 5 \times 10^{-4}$ cm^{-1} for both plots.

Appendix C. Supplementary data

Supplementary data to this article can be found online at https://doi.org/10.1016/j.optmat.2022.112404.

References

[1] R.I. Epstein, M.I. Buchwald, B.C. Edwards, T.R. Gosnell, C.E. Mungan, Observation of laser-induced fluorescent cooling of a solid, Nature 377 (1995) 500–503.

[2] S.R. Bowman, C.E. Mungan, New materials for optical cooling, Appl. Phys. B 71 (2000) 807–811.

[3] S.D. Melgaard, A.R. Albrecht, M.P. Hehlen, M. Sheik-Bahae, Solid-state optical refrigeration to sub-100 Kelvin regime, Sci. Rep. 6 (2016) 20380.

[4] M.P. Hehlen, J. Meng, A.R. Albrecht, E.R. Lee, A. Gragossian, S.P. Love, C. E. Hamilton, R.I. Epstein, M. Sheik-Bahae, First demonstration of an all-solid-state optical cryocooler, Light Sci. Appl. 7 (2018) 15.

[5] S.R. Bowman, Lasers without internal heat generation, IEEE J. Quant. Electron. 35 (1999) 115–122.

[6] S.R. Bowman, S.P. O'Connor, S. Biswal, N.J. Condon, A. Rosenberg, Minimizing heat generation in solid-state lasers, IEEE J. Quant. Electron. 46 (2010) 1076–1085.

[7] Z. Yang, J. Meng, A.R. Albrecht, M. Sheik-Bahae, Radiation-balanced Yb:YAG disk laser, Opt. Express, OE 27 (2019) 1392–1400.

[8] G. Nemova, Radiation-balanced lasers: history, status, potential, Appl. Sci. 11 (16) (2021) 7539.

[9] M.P. Hehlen, R.I. Epstein, H. Inoue, Model of laser cooling in the Yb^{3+}-doped fluorozirconate glass ZBLAN, Phys. Rev. B 75 (2007), 144302.

[10] S. Melgaard, D. Seletskiy, V. Polyak, Y. Asmerom, M. Sheik-Bahae, Identification of parasitic losses in Yb:YLF and prospects for optical refrigeration down to 80K, Opt. Express, OE 22 (2014) 7756–7764.

[11] A. Salkeld, L. Cheng, L.B. Andre, S.C. Rand, Optical Refrigeration and Saturation Effects in Oxide Crystals, 20th Int. Conf. on Dynamical Processes in the Excited States of Solids," Christchurch, NZ, August 26-30, 2019.
[12] X. Luo, M.D. Eisaman, T.R. Gosnell, Laser cooling of a solid by 21K starting from room temperature, Opt. Lett., OL 23 (1998) 639–641.
[13] S.C. Rand, Lectures on Light, second ed., Oxford University, 2016. See Eq. (5.1.29).
[14] D.E. McCumber, Einstein relations connecting broadband emission and absorption spectra, Phys. Rev. 136 (1964) A954–A957.
[15] S. Püschel, S. Kalusniak, C. Kränkel, H. Tanaka, Temperature-dependent radiative lifetime of Yb:YLF: refined cross sections and potential for laser cooling, Opt Express 29 (2021) 11106–11120.
[16] G.B. Scott, D.E. Lacklison, J.L. Page, Absorption spectra of $Y_3Fe_5O_{12}$(YIG) and $Y_3Ga_5O_{12}$: Fe^{3+}, Phys. Rev. B 10 (1974) 971–986.
[17] S.R. Bowman, Optimizing average power in low quantum defect lasers, Appl. Opt. 54 (2015) F78–F84.
[18] M. Sheik-Bahae, Z. Yang, Optimum operation of radiation-balanced lasers, IEEE J. Quant. Electron. 56 (2020) 1–9.
[19] L. Cheng, L.B. Andre, A.J. Salkeld, L.H.C. Andrade, S.M. Lima, J.R. Silva, D. Rytz, S. C. Rand, Laser cooling of Yb^{3+}:KYW, Opt. Express, OE 28 (2020) 2778–2788.
[20] E.S. de L. Filho, G. Nemova, S. Loranger, R. Kashyap, Laser-induced cooling of a Yb: YAG crystal in air at atmospheric pressure, Opt. Express, OE 21 (2013) 24711–24720.
[21] D.V. Seletskiy, S.D. Melgaard, A.D. Lieto, M. Tonelli, M. Sheik-Bahae, Laser cooling of a semiconductor load to 165 K, Opt. Express, OE 18 (2010) 18061–18066.
[22] R.L. Aggarwal, D.J. Ripin, J.R. Ochoa, T.Y. Fan, Measurement of thermo-optic properties of $Y_3Al_5O_{12}$, $Lu_3Al_5O_{12}$, $YAlO_3$, $LiYF_4$, $LiLuF_4$, BaY_2F_8, $KGd(WO_4)_2$, and $KY(WO_4)_2$ laser crystals in the 80–300K temperature range, J. Appl. Phys. 98 (2005), 103514.
[23] J. Shen, R.D. Lowe, R.D. Snook, A model for cw laser induced mode-mismatched dual-beam thermal lens spectrometry, Chem. Phys. 165 (1992) 385–396.
[24] J.R. Silva, L.C. Malacarne, M.L. Baesso, S.M. Lima, L.H.C. Andrade, C. Jacinto, M. P. Hehlen, N.G.C. Astrath, Modeling the population lens effect in thermal lens spectrometry, Opt. Lett., OL 38 (2013) 422–424.
[25] Note these results agree with those recently reported by L.B. Andre, L. Cheng, and S.C. Rand, Appl. Sci. 12 (2022) 953 (on the basis of independent TLS and DLT experiments).
[26] A.D. Lieto, A. Sottile, A. Volpi, Z. Zhang, D.V. Seletskiy, M. Tonelli, Influence of other rare earth ions on the optical refrigeration efficiency in Yb:YLF crystals, Opt. Express, OE 22 (2014) 28572–28583.
[27] G. Cittadino, A. Volpi, A.D. Lieto, M. Tonelli, Co-doping of $LiYF_4$ crystal: a virtuous effect of cooling efficiency, J. Phys. D Appl. Phys. 51 (2018), 145302.
[28] A. Volpi, J. Meng, A. Gragossian, A.R. Albrecht, S. Rostami, A.D. Lieto, R.I. Epstein, M. Tonelli, M.P. Hehlen, M. Sheik-Bahae, Optical refrigeration: the role of parasitic absorption at cryogenic temperatures, Opt. Express, OE 27 (2019) 29710–29718.
[29] B.I. Greene, R. Wolfe, Femtosecond relaxation dynamics in magnetic garnets, J. Opt. Soc. Am. B 2 (1985) 600–605.
[30] N. Pathak, S.K. Gupta, K. Sanyal, M. Kumar, R.M. Kadam, V. Natarajan, Photoluminescence and EPR studies on Fe^{3+}-doped $ZnAl_2O_4$: an evidence for local site swapping of Fe^{3+} and formation of inverse and normal phase, Dalton Trans. 43 (2014) 9313–9323.
[31] Z.V. Gareyeva, R.A. Doroshenko, Optical absorption of octahedral ions Fe^{2+}, Fe^{4+} and photoinduced effect in YIG single crystals, J. Magn. Magn Mater. 268 (2004) 1–7.
[32] J. Ma, J. Dong, K.I. Ueda, A.A. Kaminskii, Optimization of Yb:YAG/Cr^{4+}:YAG composite ceramics passively Q-switched microchip lasers, Appl. Phys. B 105 (2011) 749–760.